Investigating Exotic Phenomena of Neutron-Rich Nuclei in the Light-Mass Region Using RMF+CMR*

Meng-Jie Chen (陈梦洁)[1] Wei Zhou (周伟)[1] Tai-Hua Heng (衡太骅)[1†]

[1]School of physics, Anhui University, Hefei 230601, China

Abstract: The exploration of exotic nuclear phenomena is a central theme in nuclear physics. In this work, the exotic structures of neutron-rich phosphorus, sulfur, chlorine, and argon isotopic chains are systematically investigated using the relativistic mean field combined with the complex momentum representation (RMF+CMR) approach. Based on the calculated two-neutron separation energies, the neutron drip-line positions of the four isotopic chains are predicted. In addition, the single-particle levels of these four isotopic chains are examined. The increasing difference between the neutron and proton rms radii indicates enhanced neutron-skin character in the neutron-rich region. Finally, diffuse density distributions are observed across the P, S, Cl, and Ar isotopic chains.

Keywords: Resonant states, complex momentum representation, **Drip-line**

DOI: 10.1088/1674-1137/aeb3f5 **CSTR:**

CPC Accepted

I. INTRODUCTION

With the rapid development of experimental techniques, nuclear physics has expanded from the traditional β-stability line toward exotic nuclei near the drip line. These nuclei, characterized by extreme neutron-to-proton ratios, exhibit a variety of novel phenomena, including neutron and proton halos [1–6], the disappearance of conventional magic numbers and the emergence of new ones [7, 8], cluster structures [9], and exotic decay modes [10].

Neutron-rich isotopes of P, S, Cl, and Ar far from stability have attracted considerable attention because of the associated shell evolution and shape coexistence [11]. Precision mass measurements of the neutron-rich chlorine isotopes $^{43-45}$Cl were performed at the Low Energy Beam and Ion Trap (LEBIT) facility, providing key experimental constraints on shell closure in this region [12]. The $B(E2)$ strengths to low-lying 2^+ states in neutron-rich sulfur isotopes were extracted via intermediate-energy Coulomb excitation, mapping the evolution of quadrupole collectivity from near stability to the $N = 28$ island of inversion and testing nuclear models of collectivity [13]. The level schemes of $^{34-38}$P are crucial for understanding nuclear structure and intruder states in and around the island of inversion [14]. A recent experiment at the Radioactive Isotope Beam Factory (RIBF) measured, for the first time, the β-decay half-lives of several very neutron-rich isotopes ranging from sulfur to potassium, thereby filling a gap in the experimental database for this region [15]. Furthermore, existing experimental results provide key evidence for the $N = 32$ and $N = 34$ subshell closures in neutron-rich argon isotopes [16–19]. In parallel, extensive theoretical studies have been carried out. Using the relativistic mean-field model (RMF), Wang et al. predicted the inversion of the $2s_{1/2}$ and $1d_{3/2}$ orbitals in neutron-rich phosphorus isotopes [20]. The strength of the $N = 28$ shell closure depends strongly on proton number: the shell gap is quenched in sulfur isotopes, whereas it remains robust in argon and heavier nuclei [21]. Systematic ab initio calculations have elucidated the shell evolution and low-lying spectroscopic properties of neutron-rich sd-pf shell nuclei, providing important theoretical benchmarks for future experimental studies [22, 23]. Collectively, these experimental and theoretical efforts on P, S, Cl, and Ar isotopes provide a solid foundation for understanding shell evolution and exotic nuclear structures.

As the neutron number approaches the drip line, continuum coupling becomes crucial for describing exotic structures such as neutron halos and skins, requiring proper treatment for reliable predictions in this mass region. Various methods incorporating continuum effects have thus been developed over the past decades. For the first time, Meng and Ring identified the microscopic mechanism of neutron halo formation in ^{11}Li within the relativistic continuum Hartree–Bogoliubov (RCHB) framework [24]. Subsequent theoretical studies further predicted giant halos in the neutron-rich region [25, 26].

Received 3 July 2026; Accepted 13 October 2026

* This work was partially supported by the Nation-al Natural Science Foundation of China under Grant No.12375109

† E-mail: hength@ahu.edu.cn

©2026 Chinese Physical Society and the Institute of High Energy Physics of the Chinese Academy of Sciences and the Institute of Modern Physics of the Chinese Academy of Sciences and IOP Publishing Ltd. All rights, including for text and data mining, AI training, and similar technologies, are reserved.

DRHB studies have extended microscopic investigations of neutron halos to deformed nuclei [27]. The deformed relativistic Hartree–Bogoliubov theory in continuum (DRHBc) provides a self-consistent framework for treating deformation, pairing correlations, and continuum effects [28]. Recent DRHBc studies have further advanced the microscopic description of deformed neutron halos, covering shell evolution, p-wave halo configurations, shape decoupling, nuclear magnetism, and structure–reaction connections [29–33]. Moreover, triaxial deformation degrees of freedom are further incorporated in the triaxial relativistic Hartree–Bogoliubov theory (TRHBc), which provides a theoretical framework for studying triaxial deformation halos in Al isotopes [34, 35]. Meanwhile, resonances, which play a key role in the formation of exotic nuclei, have attracted considerable attention [36]. The complex momentum representation (CMR) method recasts resonance problems as bound-state-like eigenvalue problems by constructing an integration contour on the complex momentum plane, enabling a unified theoretical treatment of bound states, resonant states, and the continuum [37]. This method has been demonstrated to be highly reliable for studying single-particle resonances [38], and it is applicable to both spherical nuclei [39] and deformed nuclei [40]. On this basis, the RMF+CMR framework was developed and has since been widely used to describe ground-state properties of neutron-rich nuclei, yielding substantial progress in elucidating a variety of exotic phenomena. In this study, possible halo structures in the isotopic chains of phosphorus, sulfur, chlorine, and argon are systematically explored based on this theoretical framework. This paper is organized as follows. The theoretical formalism is derived in Sec. II. Numerical details and results are presented in Sec. III. Finally, conclusions are drawn in Sec. IV.

II. FORMALISM

In RMF theory, nucleons are treated as Dirac particles moving in meson and electromagnetic fields. The Lagrangian of the system is given by [41]:

$$\begin{aligned}\mathcal{L} = &\bar{\psi}\left[i\gamma^{\mu}\partial_{\mu} - M - g_{\sigma}\sigma - g_{\omega}\gamma^{\mu}\omega_{\mu} - g_{\rho}\gamma^{\mu}\vec{\tau}\vec{\rho}_{\mu}\right]\psi \\ &-\bar{\psi}\left[\frac{1}{2}e\gamma^{\mu}(1-\tau_3)A_{\mu}\right]\psi + \frac{1}{2}(\partial_{\mu}\sigma\partial^{\mu}\sigma - m_{\sigma}^2\sigma^2) \\ &-\frac{1}{4}\omega^{\mu\nu}\omega_{\mu\nu} + \frac{1}{2}m_{\omega}^2\omega^{\mu}\omega_{\mu} - \frac{1}{3}g_2\sigma^3 - \frac{1}{4}g_3\sigma^4 \\ &-\frac{1}{4}\vec{\rho}^{\mu\nu}\vec{\rho}_{\mu\nu} + \frac{1}{2}m_{\rho}^2\vec{\rho}^{\mu}\vec{\rho}_{\mu} + \frac{1}{4}c_3(\omega^{\mu}\omega_{\mu})^2 \\ &-\frac{1}{4}F^{\mu\nu}F_{\mu\nu}. \end{aligned} \tag{1}$$

In the present calculations, the NL3 parameter set [42] is adopted for the coupling constants and masses in the Lagrangian. Here, M denotes the nucleon mass, and m_{ω}, m_{σ}, and m_{ρ} denote the corresponding meson masses. The coupling constants of the ω, σ, and ρ mesons to nucleons are g_{ω}, g_{σ}, and g_{ρ}, respectively. Application of the classical variational principle yields the Dirac

$$\left[\vec{\alpha}\cdot\vec{p} + \beta(M+S) + V\right]\psi = \varepsilon_i\psi. \tag{2}$$

In this equation, $\vec{\alpha}$ and β are Dirac matrices, and S and V denote the scalar and vector potentials, respectively. To treat bound states, resonances, and continuum states in a unified manner, we transform the Dirac

$$\int d\vec{k}'\langle\vec{k}|H|\vec{k}'\rangle\psi(\vec{k}') = \varepsilon\psi(\vec{k}). \tag{3}$$

For axially deformed nuclei, the momentum-space wave function $\psi(\vec{k})$ can be separated into radial

$$\psi(\vec{k}) = \psi_{m_j}(\vec{k}) = \sum_{lj}\begin{pmatrix} f^{lj}(k)\phi_{ljm_j}(\Omega_k) \\ g^{lj}(k)\phi_{\tilde{l}jm_j}(\Omega_k)\end{pmatrix}. \tag{4}$$

With the notation $\tilde{l} = 2j - l$, the radial components are labeled f and g, and the angular part is expressed as:

$$\phi_{ljm_j}(\Omega_k) = \sum_{m_s}\left\langle lm\frac{1}{2}m_s|jm_j\right\rangle Y_{lm}(\Omega_k)\chi_{m_s}. \tag{5}$$

In complex momentum space, $Y_{lm}(\Omega_k)$ is a spherical harmonic. Meanwhile, χ_{m_s} stands for the spin wave function corresponding to the third component m_s of the spin angular momentum. Substituting (4) into (3), the Dirac equation takes the following form:

$$\begin{cases} Mf^{lj}(k) - kg^{lj}(k) \\ \quad + \sum_{l'j'}\int k'^2dk'V^{+}(l',j',p,q,l,j,m_j,k,k')f^{l'j'}(k') = \varepsilon f^{lj}(k), \\ -kf^{lj}(k) - Mg^{lj}(k) \\ \quad + \sum_{l'j'}\int k'^2dk'V^{-}(\tilde{l}',j',p,q,\tilde{l},j,m_j,k,k')g^{l'j'}(k') = \varepsilon g^{lj}(k). \end{cases} \tag{6}$$

with

$$\begin{aligned} &V^{+}(l',j',p,q,l,j,m_j,k,k') \\ &\quad = (-)^l i^{l+l'}\frac{2}{\pi}\int r^2dr[V(r)+S(r)]\,j_l(kr)j_{l'}(k'r) \end{aligned}$$

CPC Accepted

$$\sum_{ms}\left\langle lm|Y_{pq}(\Omega_r)|l'm'\right\rangle\left\langle lm\frac{1}{2}m_s|jm_j\right\rangle\left\langle l'm'\frac{1}{2}m_s|j'm_j\right\rangle,$$

$$V^{-}(\tilde{l}',j',p,q,\tilde{l},j,m_j,k,k')$$
$$=(-)^{\tilde{l}}i^{\tilde{l}+\tilde{l}'}\frac{2}{\pi}\int r^2dr[V(r)-S(r)]\,j_{\tilde{l}}(kr)j_{\tilde{l}'}(k'r)$$
$$\sum_{ms}\left\langle\tilde{l}\tilde{m}|Y_{pq}(\Omega_r)|\tilde{l}'\tilde{m}'\right\rangle\left\langle\tilde{l}\tilde{m}\frac{1}{2}m_s|jm_j\right\rangle\left\langle\tilde{l}'\tilde{m}'\frac{1}{2}m_s|j'm_j\right\rangle. \tag{7}$$

When the above equation is solved in complex momentum space, both bound-state and resonance solutions are obtained. The corresponding wave functions are then Fourier transformed to the coordinate space, where their upper and lower spinor components are expressed as:

$$\begin{cases} G^{lj}(r)/r=-i^{l+1}\sqrt{\dfrac{2}{\pi}}\int k^2dk\,j_l(kr)f^{lj}(k), \\ F^{lj}(r)/r=-i^{\tilde{l}}\sqrt{\dfrac{2}{\pi}}\int k^2dk\,j_{\tilde{l}}(kr)g^{lj}(k). \end{cases} \tag{8}$$

For more details on the theoretical formalism, see references [43].

III. NUMERICAL DETAILS AND RESULTS

Based on the theoretical formalism presented in Sec. II, we investigate neutron-rich even-N nuclei along the P, S, Cl, and Ar isotopic chains. The coordinate-space cutoff is set to $R_{\max}=14.0$ fm, which is sufficient based on convergence tests with $R_{\max}=14$, 16, 18, and 20 fm. A momentum cutoff of $k_{\max}=4.0\ \mathrm{fm}^{-1}$ and $N_c=8$ spherical configurations are employed. Pairing correlations are treated within the Bardeen–Cooper–Schrieffer (BCS) approximation using the empirical gap $\Delta=12/\sqrt{A}$ MeV for both neutrons and protons [44]. For odd-Z nuclei, the unpaired proton is treated using the blocking procedure.

The calculated two-neutron separation energies (S_{2n}) as a function of neutron number N for the P, S, Cl, and Ar isotopic chains within the RMF+CMR+BCS framework are presented in Fig. 1, together with the corresponding results without BCS pairing and available experimental data [45]. Overall, the calculated S_{2n} values decrease with increasing neutron number for all four isotopic chains. The inclusion of BCS pairing leads to a smoother evolution of S_{2n} along the isotopic chains, indicating that pairing correlations affect both the magnitude and evolution of S_{2n}. Nevertheless, both calculations predict the same neutron drip-line positions. For the P, S, Cl, and Ar isotopic chains, S_{2n} first becomes negative at $N=42$, indicating neutron drip lines at $N=40$, corresponding to ^{55}P, ^{56}S, ^{57}Cl, and ^{58}Ar, respectively. A noticeable discontinuity in S_{2n} is also observed at $N=28$ for the Ar chain, reflecting the shell effect associated with this neutron magic number. The present calculations reproduce the overall experimental trend reasonably well. However, noticeable deviations from experiment occur at $N=34$ for the Cl and Ar isotopes, where the experimental S_{2n} values decrease more sharply. These discrepancies may arise from effects not fully considered in the present calculations, such as triaxial deformation and tensor-force contributions.

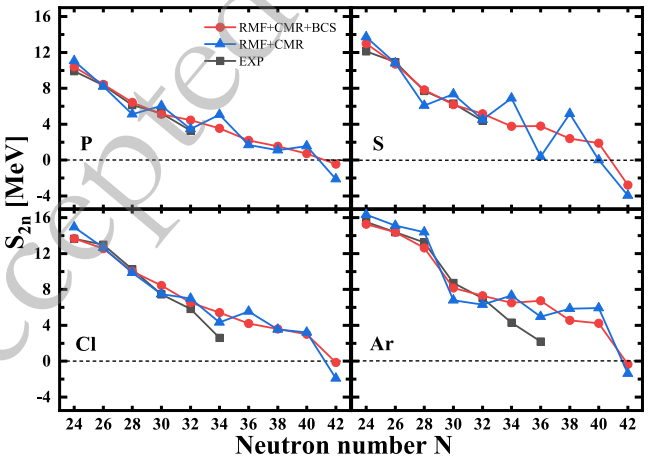


Fig. 1. (color online) S_{2n} is shown as a function of neutron number N. The red circles and blue triangles denote the results obtained with the RMF+CMR+BCS approach and without BCS pairing, respectively, while the gray squares represent the available experimental data [45].

To better investigate the exotic structures of these four neutron-rich isotopic chains, the single-neutron energy levels at selected neutron numbers are presented in Fig. 2. Different colors are used to label the quantum numbers of each orbital, and the occupancy status of the last neutron in each nuclide is indicated. The relevant energy gaps at $N=28$ are relatively weak for P and S isotones, and become more pronounced for Cl and Ar. In addition, the calculated shell gap across $N=34$ in ^{52}Ar is 1.556 MeV. Although this gap is noticeably smaller than those predicted by other theoretical models, the nonvanishing orbital energy splitting still confirms the presence of the $N=34$ subshell closure, which is consistent with the spectroscopic feature of an elevated 2_1^+ excitation energy observed in experiments [17]. The neutron Fermi energies are also indicated in Fig. 2 to clarify the binding properties of the nuclei. As the neutron number increases, the Fermi energies generally approach the continuum threshold. Importantly, the neutron Fermi energies of the drip-line nuclei in all four isotopic chains are negative, confirming that these nuclei are bound against neutron emission and supporting the drip-line positions determined from S_{2n}.

CPC Accepted

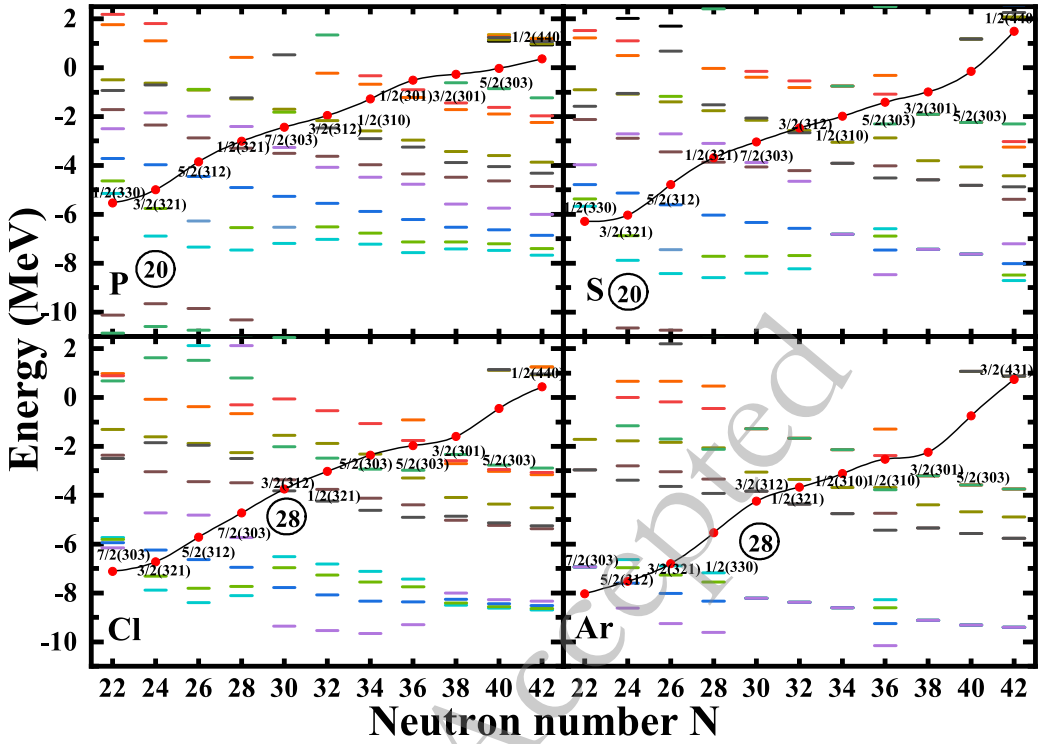


Fig. 2. (color online) The single neutron energy levels of P, S, Cl, Ar isotopes are shown as a function of neutron number *N*. The different colors are selected to mark distinct energy levels. The neutron Fermi energy is shown by the solid black curve with red dots.

CPC Accepted

The root-mean-square (RMS) radius is a fundamental observable for investigating nuclear structure. In the present work, the neutron and proton RMS radii of the P, S, Cl, and Ar isotopic chains are calculated. As shown in Fig. 3, the neutron RMS radii increase with neutron number *N* in all four isotopic chains, while the proton RMS radii vary relatively moderately. Among the four isotopic chains, the P chain exhibits a more pronounced increase toward the neutron drip line, whereas the increases in the other three chains are relatively weaker. Despite these differences, the increasing separation between the neutron and proton radii enhances the neutron-skin character of these neutron-rich nuclei.

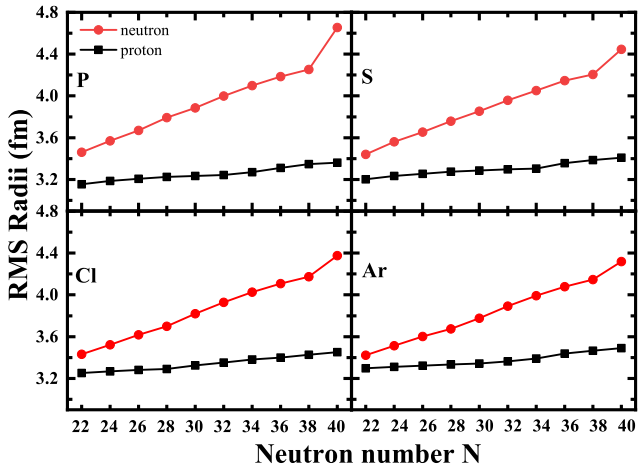


Fig. 3. (color online) RMS radius as a function of neutron number *N*. Red circles and black squares denote the neutron and proton rms radii, respectively, calculated with the RMF+CMR+BCS method.

The neutron density distributions as a function of the radial coordinate *r* for the P, S, Cl, and Ar isotopic chains are shown in Fig. 4. Different colored curves correspond to isotopes with different neutron numbers within each chain. A logarithmic scale is used on the vertical axis to highlight the tail behavior of the density distributions. Overall, the neutron density distributions of all nuclei are concentrated within a certain range of radius, but some differences can be observed among different isotopic chains and even among isotopes within the same chain. With increasing neutron number toward the neutron drip line, the neutron density distributions gradually extend to larger radial distances, and the drip-line nuclei exhibit more pronounced density tails than the lighter isotopes. To clarify the origin of this behavior, the contributions from bound and resonant states in the drip-line nuclei are shown by the blue and green dashed curves, respectively, in the insets of Fig. 4. The former decreases rapidly with radial distance, while the latter extends much farther. This indicates that the pairing-induced occupation of low-energy resonant states plays a crucial role in generating the diffuse density tail. In particular, the occupation probability of low-energy resonant states in ^{55}P is higher than

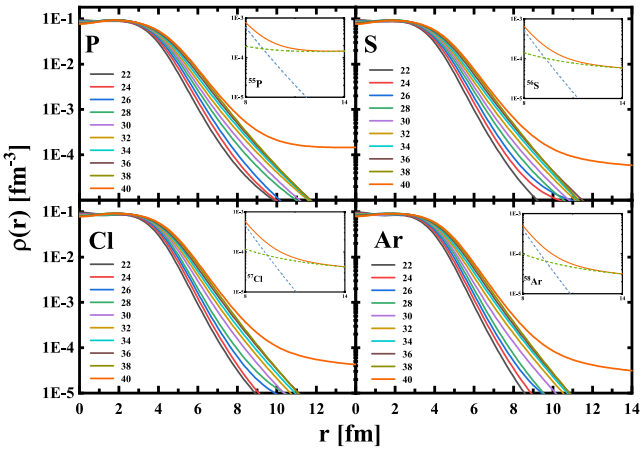


Fig. 4. (color online) The total neutron density distributions of the P, S, Cl, and Ar isotopes are presented as functions of the radial coordinate r. Isotopes with different neutron numbers N are distinguished by different colors. The insets show the decomposition of the total neutron density for ^{55}P, ^{56}S, ^{57}Cl, and ^{58}Ar, with the solid orange curves denoting the total contribution. The blue and green dashed curves denote the bound and resonant state contributions respectively.

those in ^{56}S, ^{57}Cl, and ^{58}Ar, thereby accounting for the differences in their density tails.

We also obtain the quadrupole deformation parameters β_2 for all neutron-rich nuclei, which are determined self-consistently from the converged ground-state solutions. With increasing neutron number, the calculated β_2 values show no clear pattern. The present results suggest that quadrupole deformation is not the key mechanism underlying the changes in nuclear structure properties of these neutron-rich isotopes.

IV. SUMMARY

In summary, we systematically explore the ground-state properties of even-N neutron-rich phosphorus, sulfur, chlorine, and argon isotopic chains within the RMF+CMR+BCS framework. The neutron drip lines for the four elemental sequences are determined to be at ^{55}P, ^{56}S, ^{57}Cl, and ^{58}Ar, as inferred from the evolution trend of the two-neutron separation energy S_{2n}. The single-neutron energy levels are also calculated for the four isotopic chains. The shell closure at the neutron magic number $N = 28$ is not significant in P and S, whereas it is stronger in Cl and Ar. The negative neutron Fermi energies yield the same drip-line nuclei as those identified from S_{2n}. The neutron radii generally increase toward the neutron drip line, while the proton radii remain comparatively stable. The growing difference between the neutron and proton rms radii reflects the progressively stronger neutron skin character of these neutron-rich nuclei. The neutron density distributions exhibit increasingly extended tails toward the neutron drip line. This behavior is mainly attributed to the contributions of low-energy resonant states, whose occupation probability is higher in ^{55}P than in ^{56}S, ^{57}Cl, and ^{58}Ar. The quadrupole deformation does not play a major role in the exotic phenomena arising from the significant increase in neutron number. These results may help clarify the mechanisms of structural evolution in neutron-rich nuclei near the neutron drip line and can serve as a theoretical reference for future experiments and nuclear astrophysics.

CPC Accepted

References

[1] Y. Z. Wang, F. Z. Xing, J. P. Cui *et al.*, Chin. Phys. C **47**(8), 084101 (2023)
[2] E. B. Huo, K. R. Li, X. Y. Qu *et al.*, Nucl. Sci. Tech. **34**(7), 105 (2023)
[3] H. L. Wang, Z. Wang, C. F. Chen *et al.*, Phys. Rev. C **112**(2), 024313 (2025)
[4] V. Yu. Denisov, Nucl. Phys. A **1063**, 123213 (2025)
[5] D. M. Rodkin and Yu. M. Tchuvil'sky, JETP Lett. **118**(3), 153 (2023)
[6] A. N. Abdullah, Int. J. Mod. Phys. E **31**(8), 2250076 (2022)
[7] H. H. Li, J. G. Li, M. R. Xie *et al.*, Phys. Lett. B **867**, 139609 (2025)
[8] W. Q. Ma and Y. B. Qian, Chin. Phys. C **46**(1), 014106 (2022)
[9] Y. Taniguchi, Phys. Rev. C **99**(6), 064309 (2019)
[10] Z. Y. Yuan, D. Bai, Z. Wang *et al.*, Sci. China-Phys. Mech. Astron. **66**(2), 222012 (2023)
[11] F. Sarazin, H. Savajols, W. Mittig *et al.*, Phys. Rev. Lett. **84**(22), 5062 (2000)
[12] H. Erington, G. Bollen, G. Dykstra *et al.*, Phys. Rev. C **112**(4), 044313 (2025)
[13] B. Longfellow, D. Weisshaar, A. Gade *et al.*, Phys. Rev. C **103**(5), 054309 (2021)
[14] R. Chapman, A. Hodsdon, M. Bouhelal *et al.*, Phys. Rev. C **92**(4), 044308 (2015)
[15] Q. B. Zeng, S. Nishimura, V. H. Phong *et al.*, Phys. Rev. Lett. **135**(23), 232501 (2025)
[16] D. Steppenbeck, S. Takeuchi, N. Aoi *et al.*, Phys. Rev. Lett. **114**(25), 252501 (2015)
[17] H. N. Liu, A. Obertelli, P. Doornenbal *et al.*, Phys. Rev. Lett. **122**(7), 072502 (2019)
[18] B. D. Linh, A. Corsi, A. Gillibert *et al.*, Phys. Rev. C **109**(3), 034312 (2024)
[19] M. M. Juhsz, Z. Elekes, D. Sohler *et al.*, Phys. Lett. B **814**, 136108 (2021)
[20] Z. J. Wang, Z. Z. Ren, T. K. Dong *et al.*, Phys. Rev. C **90**(2), 024307 (2014)
[21] X. W. Xia, Chin. Phys. C **40**(7), 074101 (2016)
[22] M. R. Xie, L. Y. Shen, J. G. Li *et al.*, Chin. Phys. C **48**(7), 074106 (2024)
[23] Q. Yuan, L. Y. Shen, M. R. Xie *et al.*, Chin. Phys. C **49**(9), 094104 (2025)
[24] J. Meng and P. Ring, Phys. Rev. Lett. **77**(19), 3963 (1996)
[25] J. Terasaki, S. Q. Zhang, S. G. Zhou *et al.*, Phys. Rev. C

74(5), 054318 (2006)
[26] J. Meng and P. Ring, Phys. Rev. Lett. **80**, 460 (1998)
[27] S. G. Zhou, J. Meng, P. Ring *et al*., Phys. Rev. C **82**, 011301 (2010)
[28] L. L. Li, J. Meng, P. Ring *et al*., Phys. Rev. C **85**(2), 024312 (2012)
[29] J. L. An, K. Y. Zhang, Q. Lu *et al*., Phys. Lett. B **849**, 138422 (2024)
[30] K. Y. Zhang, P. Papakonstantinou, M.-H. Mun *et al*., Phys. Rev. C **107**, L041303 (2023)
[31] K. Y. Zhang, S. Q. Yang, J. L. An *et al*., Phys. Lett. B **844**, 138112 (2023)
[32] C. Pan, K. Y. Zhang, and S. Q. Zhang, Phys. Lett. B **855**, 138792 (2024)
[33] C. Pan, J. L. An, P. Ring *et al*., Phys. Lett. B **877**, 140487 (2026)
[34] K. Y. Zhang, S. Q. Zhang, and J. Meng, Phys. Rev. C **108**(3), L041301 (2023)
[35] K. Y. Zhang, S. Q. Zhang, and J. Meng, Phys. Rev. C **112**(4), 044308 (2025)
[36] Q. Liu, J. Y. Guo, Z. M. Niu *et al*., Phys. Rev. C **86**, 054312 (2012)
[37] N. Li, M. Shi, J. Y. Guo *et al*., Phys. Rev. Lett. **117**, 062502 (2016)
[38] Y. Wang, Z. M. Niu, M. Shi *et al*., J. Phys. G **46**, 125103 (2019)
[39] S. Z. Xu, S. S. Zhang, X. Q. Jiang *et al*., Nucl. Sci. Tech. **34**(5), 1 (2023)
[40] X. N. Cao, Q. Liu, and J. Y. Guo, Phys. Rev. C **99**, 014309 (2019)
[41] P. Ring, Prog. Part. Nucl. Phys. **37**, 193 (1996)
[42] G. A. Lalazissis, J. König, and P. Ring, Phys. Rev. C **55**, 540 (1997)
[43] Y. X. Luo, Q. Liu, and J. Y. Guo, Phys. Rev. C **108**, 024320 (2023)
[44] A. Bohr and B. R. Mottelson, Nuclear Structure (Benjamin, New York, 1969), Vol. I.
[45] M. Wang, W. J. Huang, F. G. Kondev *et al*., Chin. Phys. C **45**, 030003 (2021)

CPC Accepted